Title

Climate-induced decadal ocean wave height variability from microseisms: 1931-2021

Author

Bromirski, Peter D

Publication Date

2023-08-01

Peer reviewed

JGR Oceans

RESEARCH ARTICLE
10.1029/2023JC019722

Climate-Induced Decadal Ocean Wave Height Variability From Microseisms: 1931–2021

Peter D. Bromirski[1]

[1]Scripps Institution of Oceanography, UCSD, La Jolla, CA, USA

Key Points:

- A 90-year near-coastal ocean wave record is derived from double-frequency microseisms, indicating heightened wave activity since 1970
- Extended periods of exceptionally low seismic-derived wave heights occurred prior to about 1970 when global warming accelerated
- An apparent global warming-induced intensification of the Aleutian Low is associated with more extreme waves along the California coast

Supporting Information:

Supporting Information may be found in the online version of this article.

Correspondence to:

P. D. Bromirski,
pbromirski@ucsd.edu

Citation:

Bromirski, P. D. (2023). Climate-induced decadal ocean wave height variability from microseisms: 1931–2021. *Journal of Geophysical Research: Oceans*, *128*, e2023JC019722. https://doi.org/10.1029/2023JC019722

Received 6 FEB 2023
Accepted 7 JUL 2023

Author Contributions:

Conceptualization: Peter D. Bromirski
Data curation: Peter D. Bromirski
Formal analysis: Peter D. Bromirski
Funding acquisition: Peter D. Bromirski
Investigation: Peter D. Bromirski
Methodology: Peter D. Bromirski
Project Administration: Peter D. Bromirski
Resources: Peter D. Bromirski
Software: Peter D. Bromirski
Validation: Peter D. Bromirski

Abstract Long-term coastal wave climate changes under global warming cannot be reliably assessed from relatively short duration buoy significant wave height (*Hs*) observations that began about 1980. Alternatively, microseisms at double the wave frequency (DFM) provide proxy records of near-coastal wave activity. An empirical wave reconstruction methodology transforms DFM from UC Berkeley seismic station BKS to seismic *Hs* (*sHs*). Broadband digital seismic observations since 1992 at BKS provide DFM reference spectral levels. Earlier digitized archived BKS seismogram DFM levels are adjusted to give spectral levels that are consistent with current observations, yielding a combined 90-year *sHs* record for winters (November–March) spanning the 1931–2021 epoch. Mean winter *sHs* derived from digitized 1980s seismograms are well-correlated with nearby buoy *Hs*. Comparison of deep-water extreme *Hs* with *sHs* demonstrates that *sHs* is dominated by near-coastal wave activity. Much greater decadal and interannual variability occurred during the 1931–1970 epoch, including extended periods of exceptionally low *sHs* during 1939–1947 and 1957–1965 that have not occurred since global warming accelerated near 1970, suggesting that winter extratropical storm intensity has generally increased. Comparisons of winter *sHs* variability with anomalous sea level pressure (SLPa) patterns across the North Pacific demonstrate the association of coastal *sHs* with broad-scale atmospheric variability, with differences between long-term averages of winter SLPa indicating an Aleutian Low intensification, consistent with both increased mean *sHs* and occurrence of extreme events since 1970. Recent record global annual temperatures suggest that warming may be accelerating, resulting in stronger storms that intimates further increased winter *Hs* may be forthcoming.

Plain Language Summary Heightened ocean wave activity resulting from global warming associated climate change will greatly affect coastal communities, biosystems, and infrastructure. As sea level rise progresses, the impacts of wave activity will be aggravated, resulting in increased coastal erosion and flooding of low lying regions. These issues are particularly problematic along the California coast, where vulnerable sea cliffs will experience increasing wave impacts. Because of sea level rise, projections at the end of the twenty-first century indicate that even moderate waves will produce coastal impacts comparable to recent extreme winter wave events. Seismogram records archived at UC Berkeley begin about 1930, and can be used to determine a reliable record of historic mean wave heights to assess the impact of global warming on wave activity, showing a significant change after the beginning of the upward trend in global warming near 1970, with about a doubling of extreme wave events since warming accelerated. Recent record global annual temperatures suggest that warming may be undergoing further acceleration, generating stronger storms with associated increased winter *Hs* forthcoming. The extreme storm activity across the North Pacific during the 2022–2023 winter may be a harbinger of climate change-induced heightened wave activity along the Pacific Coast.

1. Introduction

Rising sea levels exacerbate impacts of wave activity along coastlines, resulting in increased flooding, beach and sea cliff erosion, and infrastructure damage, and can affect near-coastal ecology and aquifers (Sierra & Casas-Prat, 2014; Storlazzi et al., 2000). Increased winter wave activity erodes buffering beach sands accreted during summer months, exacerbating impacts of extreme winter wave events. Impacts of wave activity along the California coast will also be exacerbated by global warming-related sea level rise, which allows more wave energy to reach vulnerable sea cliffs and coastal infrastructure. Even though storm systems tend to make landfall along more northern eastern Pacific coasts (Bromirski et al., 2016), the long period waves (swell) that they generate reach the California coast. Thus, California coastal waves are directly linked to extratropical cyclones

Writing – original draft: Peter D. Bromirski
Writing – review & editing: Peter D. Bromirski

and associated wave generation across the northeast Pacific, with their variability linked to broad-scale atmospheric patterns affected by climate change.

To assess the impact of climate change on coastal wave heights and anticipate potential future increases requires multi-decade wave records. Along the California coast, quantifying climate change related variations in wave activity are limited by the relatively short buoy record length, which begins about 1980. Ocean wave modeling efforts to characterize wave height changes rely on wind products (e.g., X. L. Wang & Swail, 2001), which are progressively less reliable prior to the advent of satellite altimetry observations in the 1980s (Timmermans et al., 2020). Wave modeling efforts thus have various sources of uncertainty to reliably assess the effect of the anthropogenic-induced upward trend in anomalous global warming (Morim et al., 2019; X. L. Wang & Swail, 2006), that began about 1970 (IPCC, 2021), on northeast Pacific wave heights. Even sophisticated models have some difficulty reliably estimating extreme *Hs* events (Ardhuin et al., 2012; Stopa et al., 2019; Stutzmann et al., 2012).

In contrast to limited observations, seismograms of wave-induced seismic signals provide a consistent platform to investigate long-term changes in near-coastal wave action (Bromirski et al., 1999). Wave-induced seismic signals include primary microseisms (PM) generated by direct wave pressure on the seafloor in shallow water (Hasselmann, 1963), and double-frequency microseisms (DFM) generated by the interaction of wave components traveling in opposite directions (Gutenberg, 1931, 1936; Longuet-Higgins, 1950). Both PM and DFM propagate as seismic Rayleigh waves. DFM have much higher amplitude than PM, yielding substantially greater signal-to-noise for wave climate investigations. Microseism variability has been linked to increased global warming (Grevemeyer et al., 2000) and to multi-decadal climate-induced coastal wave activity (Aster et al., 2008, 2010), although these efforts did not estimate associated changes in wave height. Recent efforts to estimate significant wave height (*Hs*) from DFM over extended time periods have found good correlations (Ardhuin et al., 2011, 2012; Bromirski & Flick, 2020; Stutzmann et al., 2012).

DFM source regions for individual wave events extend over 100's of km of coastline (Bromirski & Duennebier, 2002; Haubrich et al., 1963) as well as over the continental shelf (Gerstoft & Tanimoto, 2007). Because of the long-distance propagation of long-period Rayleigh waves, DFM observed on land can be generated along distant coastlines not associated with local or regional wave activity (Haubrich & McCamy, 1969), or from wave activity over the deep ocean (Ardhuin et al., 2011; Bromirski et al., 2005; Stutzmann et al., 2012), potentially contributing to land DFM levels (Gualtieri et al., 2015; Obrebski et al., 2012). However, opposing wave energy at longer periods in the deep ocean is uncertain. Additionally, propagation of DFM from the deep ocean to land is inhibited by the thinning ocean waveguide, while wave-wave interactions over the continental shelf north or south of near-coastal seismic stations can readily propagate to land (Bromirski et al., 2013). Consequently, near-coastal wave activity dominates DFM levels on land where coastal reflection provides opposing wave energy at longer periods (Bromirski & Duennebier, 2002; Stutzmann et al., 2012). Importantly, comparative spectra of near-coastal DFM and ocean swell (Bromirski & Duennebier, 2002; Bromirski et al., 1999; Haubrich et al., 1963) indicate that near-coastal seismic station DFM levels are dominated by local-to-regional near-coastal wave action, thus allowing local wave climate estimation.

Acknowledging DFM generation location and source uncertainties, here the empirical methodology of Bromirski and Flick (2020), presented in Appendix A, is applied to digitized archived seismograms to estimate changes in winter (November–March) wave activity along the central California coast. Archived seismogram digitizing considerations are described, followed by determination of instrument response adjustments needed to ensure that the spectral levels of digitized seismograms are consistent with current broadband digital data, thus allowing consistent estimates of seismic *Hs* (*sHs*) over the 1931–2021 epoch. The consistency of spectral levels and *sHs* for pre-1990 seismometers is demonstrated. Dominant near-coastal DFM source locations are inferred by comparison of *sHs* with distant deep-water and near-coastal buoy *Hs*. Decadal winter *sHs* variability is discussed for the 1931–2021 epoch. Finally, the climatological implications of the 90-year *sHs* record are inferred from winter sea level pressure (SLP) spatial patterns over the North Pacific basin associated with high and low mean winter *sHs*.

2. Data and Instrument Response Considerations

Bromirski and Flick (2020) first demonstrated the reliability of the empirical wave reconstruction methodology to estimate seismic-derived ocean *Hs* (*sHs*) over multiple decades from DFM signals recorded by the Berkeley

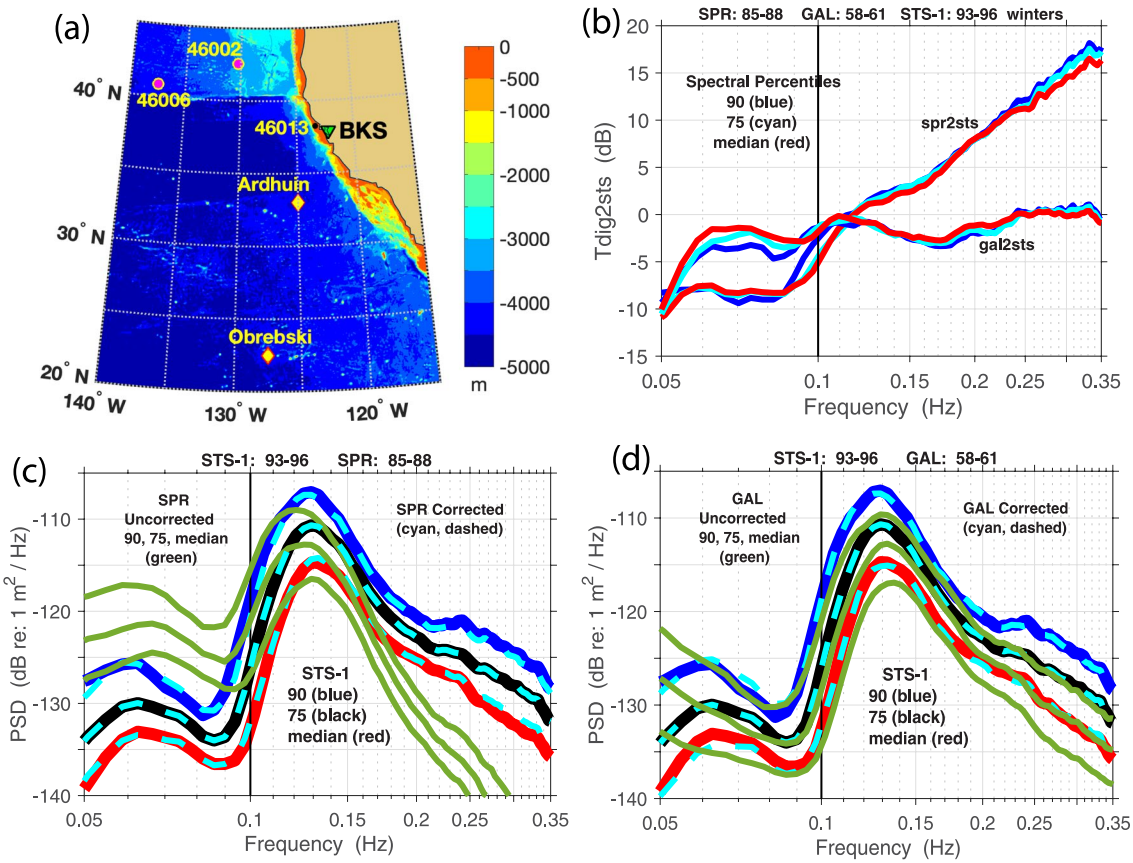

Figure 1. (a) Ocean bathymetry (depth, m) with locations of near-coastal buoy 46013 (38.238N, 123.307W, water depth 122.5 m, black dot) in relation to Berkeley, CA seismic station BKS (see Figure S1a in Supporting Information S1 for more detail). Also shown are locations of deep-water buoys 46006 and 46002, and approximate locations of strong double-frequency microseism (DFM) sources (diamonds) estimated from modeling by Ardhuin et al. (2011) and Obrebski et al. (2012). (b) Instrument response adjustment (IRA) functions *Tspr2sts* and *Tgal2sts* that adjust SPR and GAL spectra to be consistent with STS-1 for the 90, 75, and 50 (median) spectral percentile levels shown in Figure S3 in Supporting Information S1. (c) Comparison of percentile levels for uncorrected SPR (green), reference STS-1 spectra, and SPR spectra corrected with Tspr2sts. (d) Same as (c) except for GAL. Note that corrected spectra (cyan, dashed) effectively overlay STS-1 spectra (thick solid), indicating SPR and GAL spectral levels using respective IRAs will provide spectral levels, and thus *sHs*, consistent with STS-1.

Seismological Laboratory (BSL) BK network seismic station BKS using existing digital BKS seismic data. Seismic spectral estimates in the (0.1,0.45) Hz band, which spans the DFM band, combined with wave spectra and *Hs* observations at National Oceanic and Atmospheric Administration (NOAA) buoy 46013 offshore of Bodega Bay (locations in Figure 1a and Figure S1a in Supporting Information S1), yield an empirical seismic-to-wave transfer function (Figure S4 in Supporting Information S1). Reconstructed mean winter *sHs* (November-March) closely tracked mean ocean *Hs* over the 1992–2017 digital seismic record.

2.1. Archived Seismograms

Vertical component analog paper seismograms archived at UC Berkeley, CA for November–March winter seasons from November 1931 to March 1988 were scanned at 400 dpi, and then digitized at a sampling rate of 1 Hz using the trace-tracking SeisDig package (Bromirski & Chuang, 2003). Three seismometers were in sequential operation at the BK network station BKS from 1931 onward. Galitzin (GAL) seismograms were digitized for 1931–1962 winters. The transition from GAL to the Sprengnether (SPR) seismic station began in 1962. SPR seismograms were digitized for winters spanning November 1962 to March 1988, except months of GAL during January–March and December 1964. A common period when both GAL and SPR data were available spanned 11–18 December, 1964. The currently operating broadband digital STS-1 seismic station began continuous operation in 1992.

Digitizing complications included high amplitude microseisms that produced overlap between adjacent and nearby traces. High amplitude earthquake surface wave signals also result in trace overlap. Digitizing the

complete seismograms proved too costly. However, comparison tests with continuous hourly buoy *Hs* records indicated that four hourly *Hs* estimates per day (i.e., at 6 hr intervals) did not cause substantial differences in mean *Hs* estimates on monthly and seasonal time scales, although peaks of extreme events with peak *Hs* > ~6 m could be underestimated by 1–2 m. Most of the scanned seismograms were thus digitized at 1 Hz for 4 hr-long segments per 24 hr period.

2.2. Instrument Response Adjustment

To investigate mean wave height changes since 1931 employing the Bromirski and Flick (2020) methodology, DFM spectral levels for SPR and GAL must be consistent with STS-1 levels, which provided the reference levels for historic wave height reconstruction. Instrument response function poles and zeros for SPR and GAL were provided by Bob Urhammer at University of California, Berkeley (personal communication). The vertical component 1 Hz STS-1 data and its response function were downloaded from BSL online archives. The instrument response curves for STS-1, SPR, and GAL seismometers differ significantly (Figure S1 in Supporting Information S1). Instrument response-corrected vertical displacement power spectral density (PSD) levels at BKS were obtained for the three instruments using Welch averaging of 256 s segments, subsequently forming hour averages.

To obtain reconstructed *sHs* from GAL and SPR seismograms that are consistent with STS-1, their spectra need to be adjusted to approximate STS-1 levels for the wide range of spectral characteristics of winter swell events. Initially, an instrument response adjustment function for SPR, *Tspr2sts*, was estimated from the mean digitized SPR spectra and mean STS-1 spectra by forming the spectral ratio, $Tspr2sts(f) = \text{STS-1}(f)/\text{SPR}(f)$. Then the adjusted SPR spectra, SPRa, are obtained from $\text{SPRa}(f) = Tspr2sts(f) * \text{SPR}(f)$.

Initial STS-1—SPR comparisons were made using common digital records spanning a short approximately 2-day overlap interval of continuous digitized SPR and corresponding STS-1 data during 25–27 September 1991. Both show characteristic low amplitude dispersed swell-generated DFM (Figures S2a and S2b in Supporting Information S1). A constant in the SPR instrument response function was adjusted to minimize the difference between the SPR DFM (0.1, 0.15) Hz band and STS-1 levels. Application of *Tspr2sts* (Figure S2c in Supporting Information S1) yields a close match of SPRa to STS-1 levels (compare Figures S2d with S2a in Supporting Information S1). The mean levels of SPRa and STS-1 are effectively the same (Figure S2e in Supporting Information S1), indicating that associated *sHs* will be consistent. However, subsequent application of this *Tspr2sts* estimate to digitized 1981–1988 SPR spectra yielded mean winter seismic wave height estimates that significantly underestimated available buoy 46013 mean winter *Hs*. The underestimation likely results because the DFM spectra in September 1991 used to estimate *Tspr2sts* are low amplitude, strongly dispersed and narrow band, and thus do not adequately sample DFM spectral levels to provide an adequate estimate of *Tspr2sts* across the dominant DFM band from 0.1 to 0.15 Hz for high amplitude winter swell events.

Consequently, a robust estimate of *Tspr2sts* was obtained using available digitized SPR for the 1985–1988 winters (November–March) (Figure S3b in Supporting Information S1), the closest available SPR data to the SPR-to-STS-1 seismometer transition in 1992, versus STS-1 spectra for the 1993–1996 winters (Figure S3a in Supporting Information S1). The STS-1 spectra in Figure S3a in Supporting Information S1 provide the reference spectral levels that both SPR and GAL need to be calibrated against in order to determine *sHs* over the 1931–1988 epoch. Considering that the seismic sampling was nominally four hour-long samples spaced every 6 hr, using spectra spanning four winters ensures that most wave conditions that produce DF microseisms are included in estimating *Tspr2sts*. Additionally, since hourly digitized SPR time series were sampled 4 hr per day, the continuous hourly STS-1 spectral estimates were correspondingly decimated to that sample rate. The ranges of spectral variability for calibration of STS-1, SPR, and GAL are shown in Figure S3 in Supporting Information S1. The sampling employed yielded more than 2000 spectra over four winters for STS-1, SPR, and GAL data, providing robust percentile spectral estimates of DFM variability.

The 90, 75, and 50 (median) STS-1 and SPR percentile spectra (Figure 1c) were used to form *Tspr2sts* (Figure 1b). The small differences in spectral levels between adjusted SPR (Figure 1c, cyan dashed) that closely overlay associated STS-1 percentiles (thick curves) indicate that SPRa spectra give a good representation of mean DF microseism levels, and indicate that associated mean ocean wave heights estimated from the digitized SPR data will be consistent with those determined for STS-1 over 1992–2021.

Tgal2sts was obtained similarly from the spectral ratio of the GAL percentile spectra obtained for 1958–1961 winters (Figure 1d) with the same 1993–1996 STS-1 reference percentiles used to obtain *Tspr2sts*. Similar to

SPR, application of *Tgal2sts* in Figure 1d yields adjusted spectral levels, GALa, (cyan dashed) that closely overlay STS-1 levels (thick curves). Thus, both GALa and SPRa spectral levels will be consistent with STS-1, with the transformation to *sHs* allowing direct comparison of mean winter wave *sHs* over the 1931–2021 epoch.

The similarity of both the SPR and GAL instrument response adjustment functions (Figure 1b) for the different percentile levels in Figures 1c and 1d attests to their consistency, and indicates that the DFM percentile spectral levels are well-sampled. The much smaller amplitude *Tgal2sts* adjustment than *Tspr2sts* follows from the greater similarity of uncorrected GAL spectral levels to STS-1 (compare Figures 1c and 1d [green curves] with STS-1 levels [thick curves]).

2.3. Comparisons of *sHs*: SPR With STS-1 and GAL With SPR

The empirical methodology of Bromirski and Flick (2020) (Appendix A) to estimate seismic *Hs* (*sHs*) from hourly-averaged DFM spectra was employed. SPRa and GALa spectral levels were adjusted to be consistent with STS-1 using *Tspr2sts* and *Tgal2sts*, respectively, allowing application of *Tws* and *Tsw* from *Bromirski and Flick* to both SPRa and GALa, giving *sHs* that are consistent with STS-1 *sHs*. Both *Tws* and *Tsw* (Figure S4 in Supporting Information S1) were referenced to buoy 46013 wave spectra (46013 location in Figure 1a), which must be determined separately for other near-coastal seismic station/buoy pairs, for example, for nearshore buoy 46026 (locations of 46013 and 46026 in Figure S1a in Supporting Information S1). Bromirski and Flick (2020) showed that *sHs* for 46013 and nearshore buoy 46026 over the 1992–2017 BKS STS-1 epoch are well-correlated with respective *Hs* at the two buoys, demonstrating the applicability of the empirical methodology to reliably estimate *Hs* variability at various near-coastal buoys close to land seismic stations.

The consistency of the empirical methodology is demonstrated in Figure 2a for time periods when both 1 Hz digitized SPRa and continuous 1 Hz STS-1 were available. Welch-averaged spectra were obtained for a short overlapping 2-day time period in September 1991, with their 75th percentile *Tspr2sts* (Figure 1b) adjusted spectral DFM peaks near 0.13 Hz differing by about 3 dB (Figure 2a). This difference largely results from the inclusion of the much higher levels of SPR DFM employed to determine *Tspr2sts* during 1985–1988 than were present during the much shorter record in 1992, overly enhancing SPRa spectral levels at DFM frequencies.

The wave-to-seismic spectral adjustment function, *Tws* (Figure S4a in Supporting Information S1), that in part adjusts spectral levels for propagation effects of DFM Rayleigh waves from their generation region to BKS, was applied to SPRa and GALa spectra, followed by application of the *Tsw* seismic-to-wave transfer function (Figure S4b in Supporting Information S1), giving *sHs*. Tests on SPR seismograms over the 1982–1988 winters (discussed below) showed that *sHs* estimates using *Tspr2sts* for the 75th percentile SPRa spectra produced *sHs* that more closely track STS-1 *sHs*, slightly better than either the median or 90th percentile spectra. *Tspr2sts* (75th percentile, Figure 1b) was subsequently used for all SPR *sHs* reconstructions. Application of *Tws* and Tsw to the common September 1991 seismic observations yielded small differences between SPRa and STS-1 *sHs* (Figure 2b), with their means differing by <1%.

Digitized GAL and SPR seismograms were both available for the 11–18 December, 1964 period, with four approximately evenly spaced segments of 1 hr duration digitized per each 24 hr period. Similar to SPR, *Tgal2sts* from 75th percentile spectra was applied to GAL spectra obtained for four winters 1958–1961 prior to the overlap time period. Initial application of the *Tgal2sts* adjustment to the 1964 GAL spectra yielded GAL *sHs* that were significantly higher than SPR *sHs*. The SPR *sHs* for the December 1964 time period were used as the reference *sHs* for calibration of GAL *sHs* since the SPR *sHs* amplitudes were validated against buoy 46013 *Hs* observations. A constant scale factor, SF, determined by iteration, was found to be adequate to minimize the December 1964 difference | mean(SPR *sHs*)—mean(GAL *sHs*) |, giving *Tgal2sts* = SF * *Tgal2sts*, with SF = 0.44 applied to the spectral ratio of GAS 1958–1961 with STS-1 1993–1996.

Application of the SF-scaled *Tgal2sts* from 1958 to 1961 to GAL and *Tspr2sts* to the December 1964 SPR spectra produced percentile spectral levels for the 8-day period that differed only slightly (Figure 2c), with correspondingly similar *sHs* that show consistent variability (Figure 2d), giving about a 2% difference in mean *sHs* amplitude. GAL spectral distributions for different time periods are similar, for example, for 1952–1955 winters shown in Figures S9a and S9b in Supporting Information S1, as would be expected since DFM result from ocean waves that have similar patterns of spectral variability (Bromirski et al., 1999). *Tgal2sts* from GAL spectra spanning 1952–1955 winters yielded GAL *sHs* that tracked December 1964 SPR *sHs* (Figure S9d in Supporting

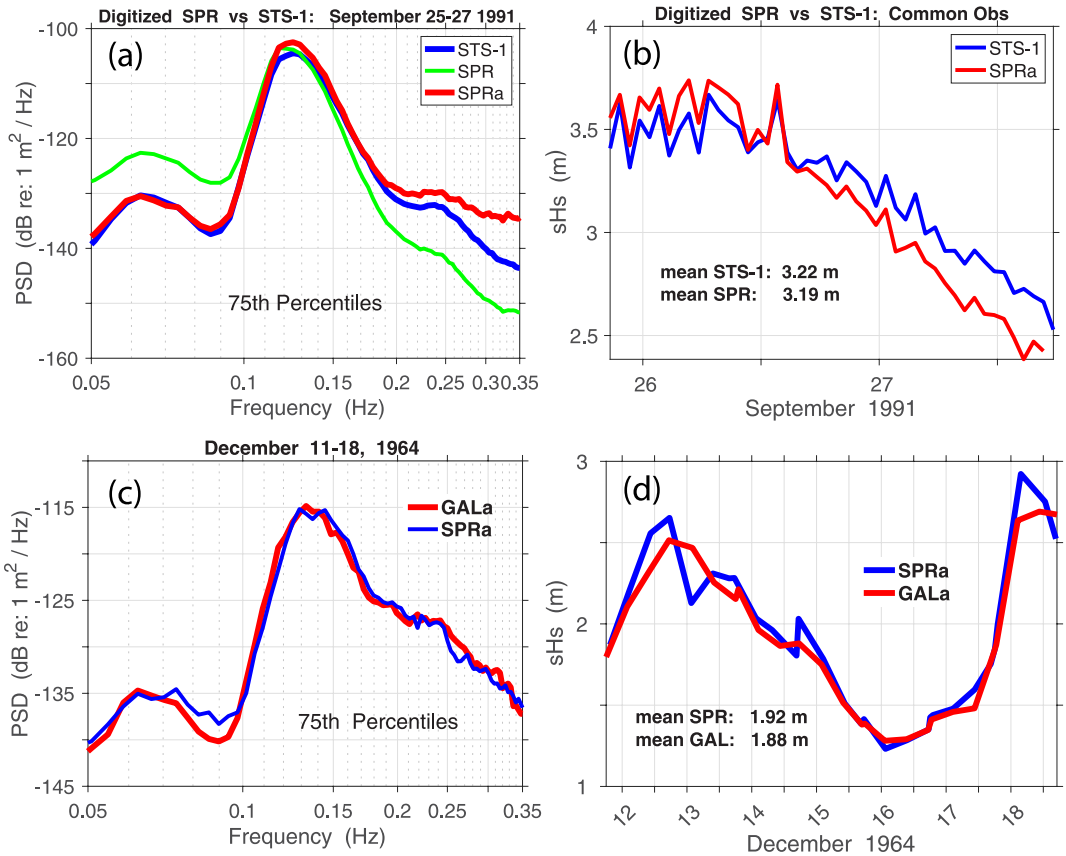

Figure 2. (Top) Spectral estimates for common observations of STS-1 and SPR spanning 25–27 September 1991, and (bottom) for SPR and GAL spanning 11–18 December, 1964. (a) 75th percentile spectra for STS-1 (blue) and digitized SPR (green), with *Tspr2sts* applied giving SPRa (red). (b) Seismic *Hs* (*sHs*) determined for hourly averaged STS-1 and SPRa spectra. (c) GALa (*Tgal2sts* applied) and SPRa (*Tspr2sts* applied) for available common observations in December 1964. (d) *sHs* determined for 4 sample/day time series for SPRa (blue) and GALa (red), both relative to STS-1 1993–1996 spectral levels.

Information S1) and winter GAL *sHs* 1931–1960 (Figure S9e in Supporting Information S1), indicating that obtaining *Tgal2sts* is largely insensitive to the choice of time period employed, although scaling of the *Tgal2sts* to account for variable DFM percentile spectral levels during different time periods would generally be needed.

Figures 2b and 2d indicate that although differences between digitized SPR and GAL *sHs* can occur on short time scales, mean *sHs* are consistent. Thus, application of respective adjustment functions will produce mean DFM spectral levels from 1931 to 1988 for digitized SPR and GAL that are consistent with current post-1992 mean STS-1 spectral levels, validating the application of the Bromirski and Flick (2020) empirical methodology. Because near-coastal buoy *Hs* estimates are directly linked to near-coastal DFM spectral levels, the pre-1990 *sHs* estimates from digitized SPR and GAL spectra, that are corrected to the STS-1 reference levels, will give *sHs* that are consistent with STS-1 *sHs*. This consistency of spectral level variation and resulting *sHs* allows investigation of long-term changes in mean winter ocean *Hs* from 1931 to 2021.

2.4. Comparison of Seismic *Hs* (*sHs*) With Winter Buoy *Hs* Since 1982

SPR seismograms were scanned and digitized (four approximately evenly-spaced hours per 24 hr period) for the 1982–1988 winters, when NOAA buoy 46013 was nominally in service. *Tws* and *Tsw* were applied to SPRa spectra. Mean winter *sHs* and *Hs* were determined for SPR and 46013, respectively. Generally, relatively small differences between mean winter *sHs* and *Hs* are observed (Figure 3a). Comparisons between *sHs* and *Hs* were complicated by occasional missing *sHs* spanning 1–2 days, and further complicated by missing *Hs* at 46013 during December and January 1981–1982, during February and March 1983 and 1986, and much of the 1988

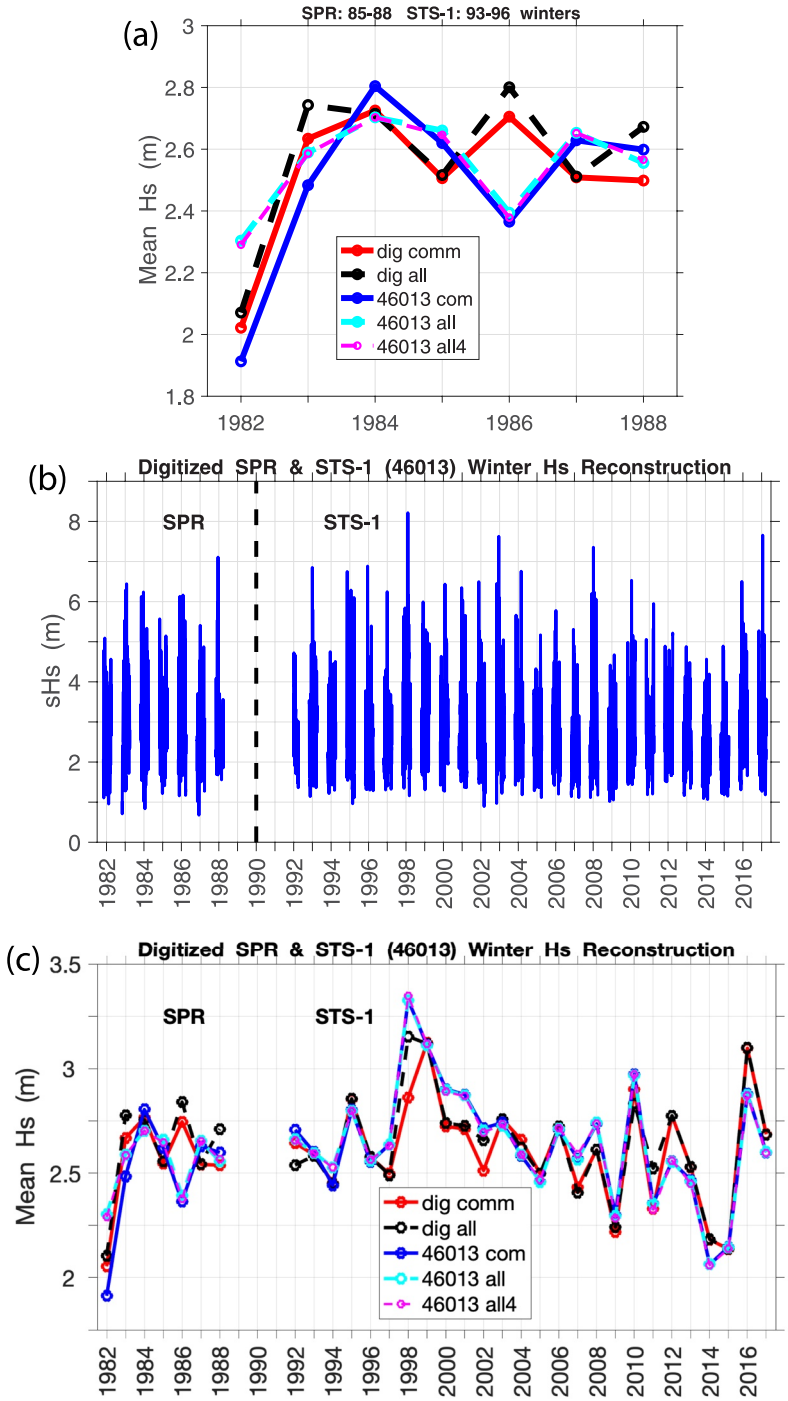

Figure 3. (a) Mean winter SPR *sHs* that spans the period when *Hs* at buoy 46013 are available during the 1982–1988 winters (e.g., the 1982 winter includes November 1981 to March 1982 wave heights). Shown are mean *sHs* for SPR hourly observations that are common with 46013 *Hs* (red), all available SPR *sHs* in each winter (black, dashed), winter 46013 *Hs* that are common with SPR *sHs* observations (blue), mean *Hs* for all 46013 winter observation (cyan), and mean 46013 winter *Hs* determined for *Hs* decimated to 4 *Hs* observations per 24 hr matching the nominal digitized SPR sample rate (magenta, dashed). (b) Hourly *sHs* for digitized SPR during the 1982–1988 winters. (c) Same as (a) with the inclusion of 1992–2017 STS-1 *sHs*.

winter. Note that decimating 46013 *Hs* to four 1-hr samples/24 hr (dashed magenta) yields mean winter *Hs* estimates that are effectively indistinguishable from estimates using all hourly *Hs* (cyan, appears dashed).

Current BKS broadband STS-1 seismic observations show that winter SPR *sHs* variability during the 1980s is similar to STS-1 *sHs* variability from 1992 to 2017 (Figure 3b). Good correlations between mean winter *sHs* and 46013 *Hs* (Figure 3c) for common observations of SPR *sHs* over 1982–1988 winters (correlation coefficient $R = 0.72$) and between 46013 *Hs* and STS-1 *sHs* over 1992–2017 ($R = 0.79$), with the difference in R likely due to the more complete and continuous STS-1 record. However, for the mostly complete 1983–1984 winter for SPR *sHs* and 46013 *Hs*, the means of common observations of were both 2.80 m, indicating that differences between buoy *Hs* and reconstructed *sHs* are small over sufficiently long and sufficiently complete records.

Wave climate variability along the Pacific coast of North America from buoy observations since the early 1980s to 2010 show no substantial trends (Gemmrich et al., 2011), consistent with *sHs* in Figures 3c and 5b. Key winters having elevated wave activity, such as the 1998 and 2016 El Niños, and low *sHs* during the 2014 and 2015 winters when persistent high atmospheric pressure systems over the eastern North Pacific impeded wave generation, attest to the consistency of BKS DFM levels with near-coastal wave activity along the California coast.

These results indicate that digitized SPR *sHs* provide a good estimate of winter wave activity. Buoy 46013 *Hs* gives a point measurement of sea state, while *sHs* is derived from DFM that result from local-to-regional wave activity and thus provide a regional average. Although no buoy records are available during the GAL seismogram epoch, the consistency between mean SPR and STS-1 *sHs* with mean winter 46013 *Hs* 1982–2017 (Figure 3), and the consistency between SPR and GAL *sHs* during December 1964 (Figure 2), indicate *sHs* from 1931 to 2021 provide reliable estimates of mean wave activity along the central California coast.

3. Importance of Non-Local DFM Sources to *sHs* Estimates

To have confidence that the *sHs* estimates are representative of wave activity along the central California coast, the importance of non-local DFM sources needs to be ascertained. Wave-wave interactions generating DFM occur throughout ocean basins, both in the deep ocean (Bromirski et al., 2005) and in near-coastal waters (Bromirski & Duennebier, 2002; Haubrich et al., 1963; Haubrich & McCamy, 1969). In the deep ocean, opposing wave energy can result from waves originating from multiple storm systems (Ardhuin et al., 2011; Obrebski et al., 2012), as well as under individual storms (Traer & Gerstoft, 2014). DFM generated on the continental shelf predominantly contribute to BKS DFM levels. However, there is some question of how much DFM energy reaches land from deep ocean regions (Bromirski et al., 2013).

At near-coastal locations, opposing waves result from shore-reflected wave energy (Bromirski & Duennebier, 2002; Haubrich et al., 1963; Stutzmann et al., 2012). Wave reflection depends on wave period and wave azimuth, and on beach slope, width, and composition (Elgar et al., 1994), with reflected amplitudes being greater for longer periods. Additionally, beach characteristics can change over the course of the winter, with buffering beach sands accreted in summer progressively being eroded during winter. Coastline geometries cause certain beaches to be more exposed to northern versus southern wave azimuths. Wave propagation to the shore is affected by nearshore bathymetry. Thus, coastal reflection coefficients are difficult to estimate (Guerin et al., 2022), and can vary substantially alongshore and are necessarily dependent on location and time of year, as well as swell characteristics. These factors all affect opposing wave component amplitudes, and thus the generation of associated near-coastal DFM signals by the shore reflection mechanism.

Because of basin-wide wave activity and significant uncertainty in estimating opposing wave fields, source locations of DFM observed at land seismic stations are broad and difficult to determine. The contribution of remote deep-ocean DFM sources to land seismic DFM levels have been modeled for particular DFM events by Ardhuin et al. (2011) and Obrebski et al. (2012), with estimated locations of their modeled DFM source areas indicated in Figure 1a. Comparison of BKS *sHs* with nearby 46013 *Hs* for these events (Figures 4a and 4b, respectively) shows *sHs* leading *Hs*, indicative of DFM being generated at a more distal location prior to the swell arriving near BKS. Also, because the empirical methodology employed here tends to underestimate *Hs*, the atypical higher *sHs* amplitudes for these events are consistent with the relatively strong non-local DFM generation identified in *Obrebski et al.* and *Ardhuin et al.*, although contributions from wave interactions resulting from shore-reflected waves along stretches of coastline farther north or south of BKS cannot be completely discounted.

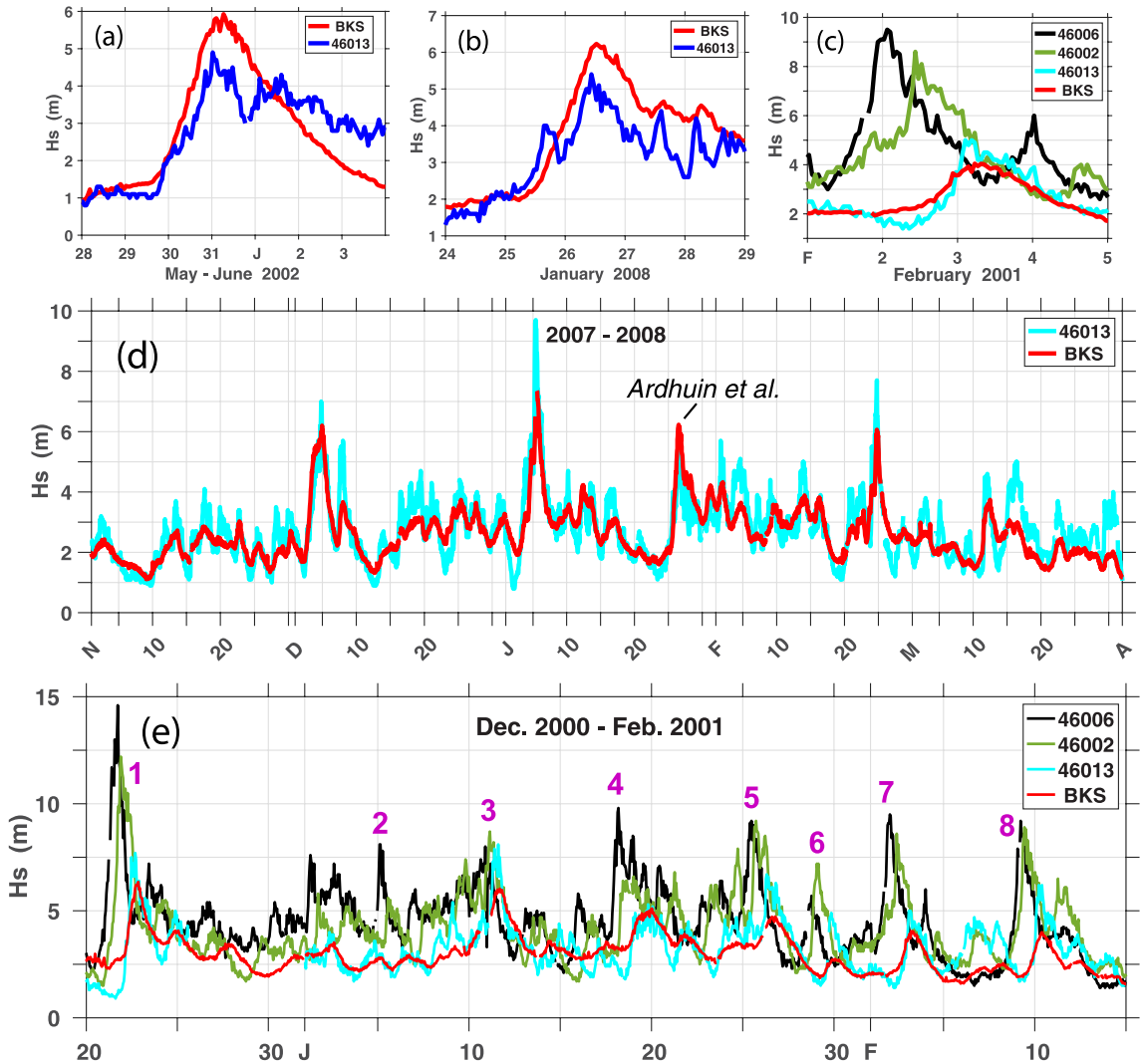

Figure 4. BKS reconstructed *sHs* and nearby buoy 46013 *Hs* for events studied in (a) Obrebski et al. (2012), (b) Ardhuin et al. (2011) (and in d), and (c) for an extreme deep-water event (# 7 in e). (d) *sHs* and 46013 *Hs* co-variability during the 2007–2008 winter. (e) Comparison of BKS *sHs* and nearby continental shelf 46013 *Hs* with *Hs* at distant deep-water buoys 46006 and 46002 during a 2-month sequence of energetic storm events producing extreme waves over the deep ocean (see Figure 1a for buoy locations).

The *Obrebski et al.* DFM event resulted from deep-ocean interactions of southward propagating extratropical swell with northward propagating waves from hurricane Alma in late October 2002, with opposing wave interactions occurring approximately 1,800 km southwest of BKS (Figure 1a). Since hurricanes typically do not occur during winter months (November–March), these types of anomalous events will generally not be a factor in mean winter *sHs* estimates. Comparison of *sHs* spanning the 2008 winter with 46013 *Hs* (Figure 4d) shows that *sHs* typically underestimates near-coastal 46013 *Hs*, with the exception of the event studied by *Ardhuin et al.*, indicating that high amplitude non-local DFM generation during this winter was atypical and that these types of events will not significantly affect mean winter *sHs*.

The potential for deep-water DFM generation biasing mean winter near-coastal *sHs* was further investigated for a particularly energetic period during the 2001 winter (Figure 4e). Several extreme *Hs* events observed at deep-water buoys 46006 and 46002 are identified (buoy locations in Figure 1a). The relationship between *Hs* at these buoys and near-coastal 46013 with *sHs* from BKS seismic data is demonstrated for a storm wave event in Figure 4c, showing that *sHs* is much more closely aligned with near-coastal 46013 *Hs*. Spectral peaks in Figures 1c and 1d are at about 0.13 Hz, giving an average period of about 15 s. Waves from large storms generally have lower frequency peak spectra, about 0.11 Hz, giving 18 s period waves. Peak *Hs* at 46013 lags 46006

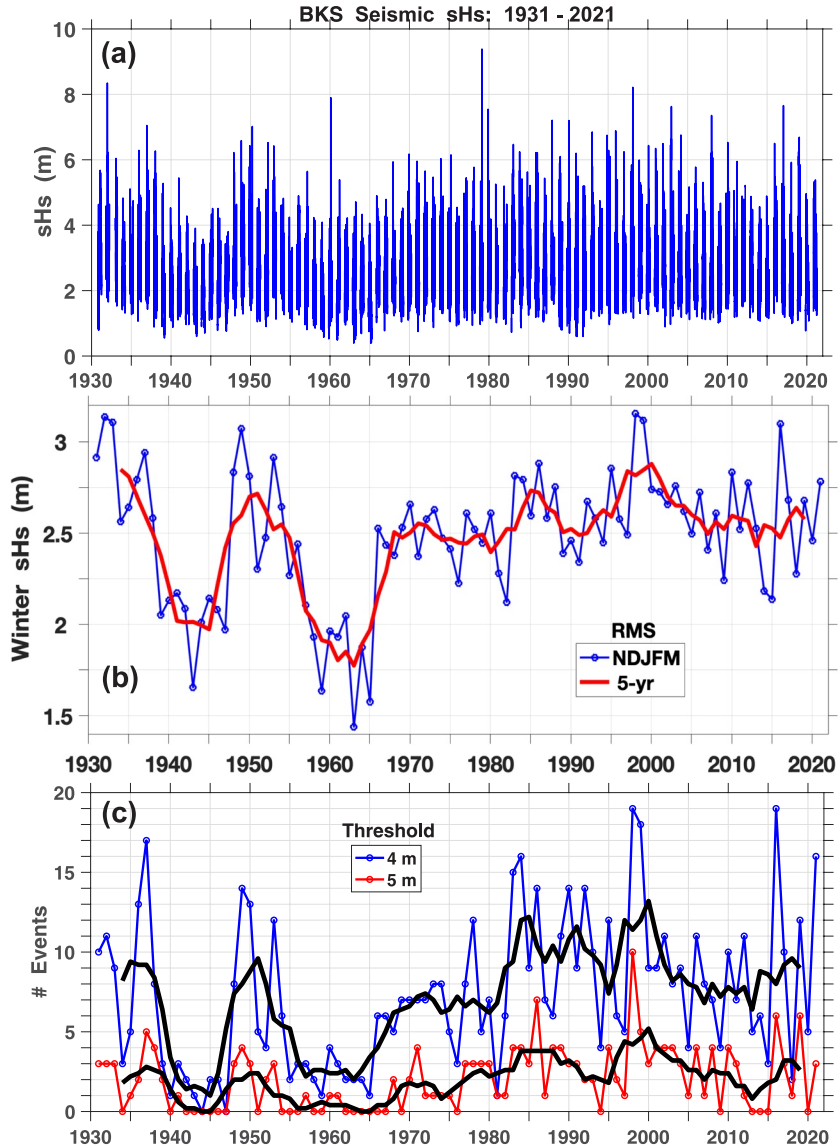

Figure 5. (a) Seismic *Hs* (*sHs*) hourly time series spanning 1931–2021. (b) Winter (November–March) *rms sHs*, with 5-year running winter *rms* (red). Buoy 46013 *Hs* were inserted for the 1989–1992 winters when digitized SPR seismograms were not available. (c) Number of *sHs* events exceeding 4 and 5 m thresholds during respective winters, with 5-year running means (black).

peak *Hs* by about 1 day (Figure 4c) for typical deep-water event #7 in Figure 4e, consistent with gravity wave propagation of about 18 s swell from 46006 to 46013. Importantly, it is clear that *sHs* is closely associated with 46013 *Hs*, and not with high amplitude deep-water wave activity, although open ocean-generated swell clearly reaches the coast. Rayleigh wave travel time from 46006 and 46002 to BKS is much less than an hour. The lack of corresponding elevated BKS *sHs* near high amplitude *Hs* at 4006 and 46002 indicates that contributions to DFM levels at BKS from the area of these deep-water buoys near peak event *Hs* is minimal, if any. This strongly suggests that opposing wave energy at long-period swell frequencies at deep-water locations that produce DFM that could reach land is typically not present, with propagation of shorter period DFM from the deep-ocean to land impeded by the thinning oceanic waveguide (Bromirski et al., 2013). Thus, DFM that would produce substantial contributions to BKS *sHs* are generally not generated in the deep ocean, but are instead most representative of wave activity over the continental shelf.

Although the wave events enumerated in Figure 4e undoubtedly have different spectral characteristics and wave azimuths, they consistently provide minimal contributions to BKS *sHs*. *sHs* peaks typically lag *Hs* at deep-water

46006 and 46002, and are, conversely, closely associated in time with near-coastal 46013 *Hs*. *sHs* generally does not exceed near-coastal *Hs* at 46013 at the time of the extreme deep-water wave events observed at 46006 and 46002 in Figures 4c and 4e. These associations indicate that DFM at BKS, and therefore *sHs*, are dominated by relatively nearby near-coastal wave interactions. Consequently, mean winter *sHs* determined from BKS DFM will not be significantly affected by non-locally generated DFM.

4. Decadal *sHs* Variability: 1931–2021

The consistent BKS spectral levels determined over the combined 90 years seismogram record allows investigation of winter (November–March) *sHs* decadal variability along the California coast. *Tgal2sts* and *Tspr2sts* adjustment functions were applied to all respective GAL and SPR data, followed subsequently by application of *Tws* and *Tsw*, giving *sHs* over the 1931–1988 epoch, with STS-1 *sHs* appended for 1993–2021 winters (Figure 5a). Buoy 46013 *Hs* were inserted for the 1989–1992 winters when digitized SPR seismograms were not available.

The winter *sHs* variability observed during the GAL and SPR epochs prior to 1989 is similar to and consistent with that observed in *sHs* and *Hs* since 1992. High amplitude *sHs* events occur prior to 1980, for example, during 1932, 1937, 1950, 1960, and 1979 and other winters, demonstrating that extreme events can occur during any winter. More pronounced decadal variability is observed during the 1931–1970 epoch, with extended periods of exceptionally low *sHs* from 1939 to 1947 and 1957–1965.

Winter *sHs* have elevated levels during the early to mid-1930s and during the late 1940s to early 1950s when GAL was in operation (Figure 5b), with elevated mean *sHs* comparable to that during the great 1997–1999 ENSO and the 2016 El Niño. The fact that both very high and very low winter *sHs* occurred under GAL provides confidence that the *sHs* variability observed is not an artifact of either the processing, which was consistently applied, or issues with instrument sensitivity, which would be unlikely to vary substantially over extended periods as both the GAL and SPR seismometers were calibrated regularly to ensure accurate earthquake amplitudes (Bob Urhammer, personal communication). Although there were several instances when *sHs* were not available, Figure S5 in Supporting Information S1 shows that missing data do not appreciably affect characterizations of interannual and decadal mean winter wave height variability.

As might be expected, the occurrence of high amplitude *sHs* events is generally more common during winters when mean *sHs* is high, with fewer strong events when mean *sHs* is low (Figures 5a and 5c). Winters with few strong events are much more prevalent prior to 1970.

5. Discussion: Climatological Associations

Climate change-associated global warming is anticipated to cause intensified storm activity, characterized by steeper extratropical cyclone (ETC) SLP gradients that cause heightened ocean wave activity over the North Pacific (Reguero et al., 2019). Extreme waves near high tide produce the greatest coastal impacts. However, under global warming-associated sea level rise, even moderate wave events at the end of the century could produce coastal impacts as great as recent extreme storm events (Cayan et al., 2008). Although *sHs* was determined for wave activity along the California coast, Figures 4c and 4e show that there is a strong association with wave activity, and hence storminess, over the eastern North Pacific, and potentially over the entire extratropical portion of the basin.

Seismic reconstructed winter *sHs* are well-correlated with buoy *Hs* (Figure 3), tracking heightened activity during the 1998 and 2016 El Niños, and low activity during the 2014 and 2015 winters. Typically, higher waves result from deeper low pressure systems, yielding higher *sHs* at BKS. The connection between *sHs* and SLP was investigated employing NOAA National Centers for Environmental Prediction (NCEP) reanalysis SLP beginning in 1948, obtained from the NOAA National Climate Data Center (NCDC). The climatological associations of these winters and implications of winter *sHs* variability over the 90-year record can be inferred from winter NCEP reanalysis SLP spatial patterns. Mean anomalous winter SLP over the North Pacific can illuminate atmospheric patterns associated with heightened or depressed winter *sHs*. Anomalous SLP (SLPa) were determined as the difference between the reanalysis SLP long-term monthly mean at each grid node and their monthly means.

The Oceanic Niño Index (ONI, NOAA Climate Prediction Center) and the Multivariate Enso Index (MEI; Wolter & Timlin, 2011) indicate that very strong El Niños since 1950 occurred during the 1982–1983, 1997–1998, and

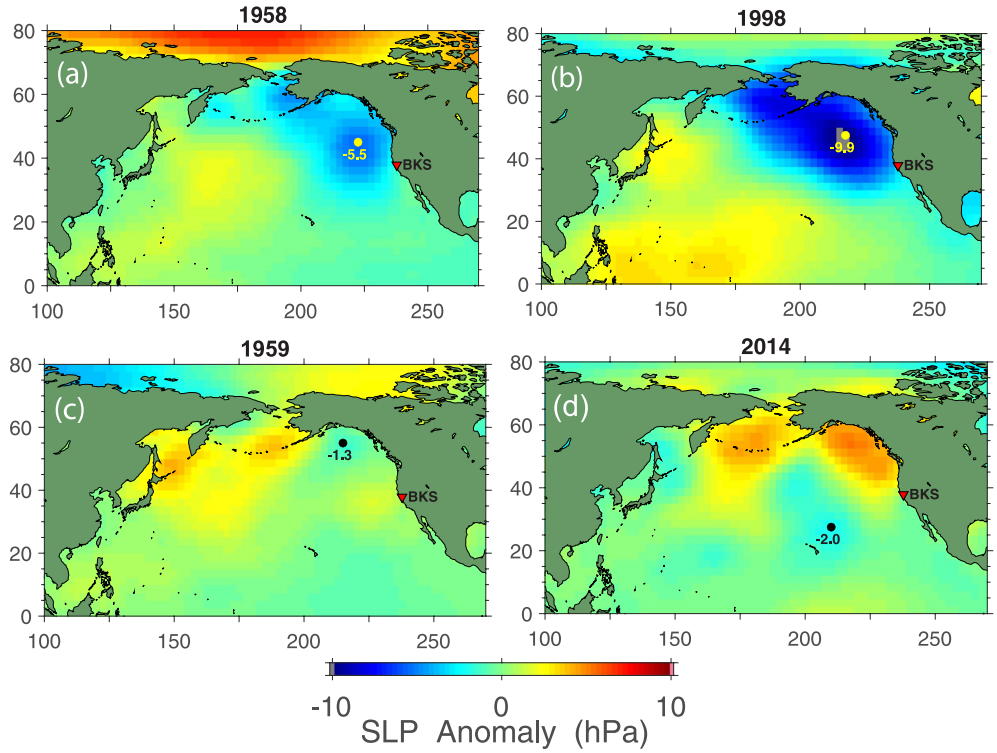

Figure 6. Mean winter (November–March) anomalous sea level pressure (SLP) patterns across the North Pacific for (a) and (b) El Niño winters, and (c) and (d) low *sHs* winters (see Figure 5b). The magnitude and location of the deepest mean anomalous low SLP during each winter are indicated (years are associated with the January–March months).

2015–2016 winters, with moderate to strong El Niño in 1957–1958 and 1940–1941 winters. Representative El Niño winters both before and after the advent of the upward trend in anomalous global surface temperature near 1970 (IPCC, 2021) were selected (1958 and 1998, respectively) to examine the association of *sHs* at BKS with North Pacific mean winter SLPa patterns (Figures 6a and 6b, respectively). Both patterns have respective deepest SLPa lows centered in the northeast Pacific, with a deeper more extensive low during 1998 consistent with both the stronger ONI and higher mean winter *sHs* than during 1958. The 1983 and 2016 El Niños have SLPa patterns similar to 1998.

Similarly low mean winter *sHs* during the 1958 and 1941 El Niños are consistent with similar MEI values for those winters. Correspondingly, low mean *sHs* during the 1959 and 2014 winters have characteristically higher mean SLPa (Figures 6c and 6d), with associated pressure patterns that are not conducive to strong pressure gradients that produce high winds that lead to generation of high amplitude waves. High winter *sHs* can occur in non-ENSO winters, for example, 1949 (Figure 5b), when a deep Aleutian Low persisted for most of the winter months (Figure S6 in Supporting Information S1). Together, the SLPa pressure patterns in Figure 6 and Figure S6 in Supporting Information S1 demonstrate the close association of *sHs* wave activity along the California coast with climate-related atmospheric variability across the North Pacific.

The 5-year running mean (Figure 5b, red curve) shows quasi-decadal *sHs* variability, with an apparent change in decadal-scale patterns after about 1970. Multi-year periods of very low *sHs* have not occurred after 1970. Mean winter *sHs* since 1970 increased by about 13% compared with the 1931–1969 epoch. Aster et al. (2010) and Grevemeyer et al. (2000) also inferred a post-1970 global warming-associated increase in wave heights over the North Atlantic from microseismic data, indicating that increased ETC intensity associated with climate change occurred over boreal ocean basins. The absence of successive multi-winter very low winter wave levels after 1970 also suggests that winter ETC intensity has generally increased.

To assess decadal changes in atmospheric patterns associated with increased ETC intensity, winter SLPa were averaged over 20 years epochs from 1949 to 1969 (Figure 7a) and 1996 to 2016 (Figure 7b). The 1955–1965 low wave period in the earlier epoch strongly influences the high SLPa region near the Aleutians, while the Aleutian Low SLPa pattern in the latter epoch is affected by the inclusion of the 1998 and 2016 strong El Niño winters.

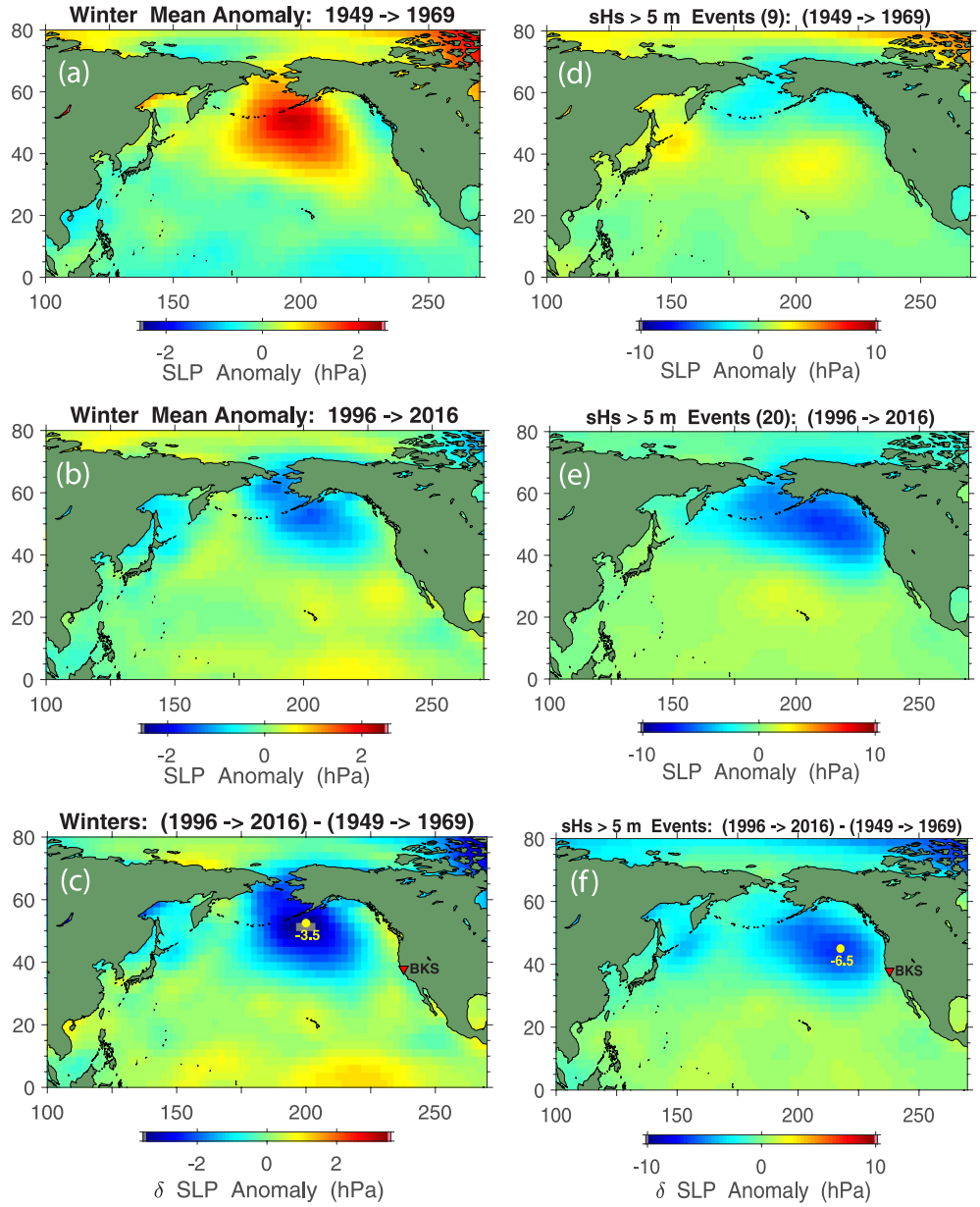

Figure 7. (a) Mean winter sea level pressure anomalies (SLPa) averaged over November–March for the 1949–1969 winters. (b) Same as (a) except over the 1996 to 2016 winters. (c) SLPa difference between (a) and (b). (d) Mean SLPa anomalies averaged for 9 months when extreme *sHs* wave events occurred during winter over the 1949–1969 epoch (see Figure S8 in Supporting Information S1 for the extreme event occurrence). (e) Same as (d) except for 20 months over the 1996 to 2016 epoch. (f) SLPa difference between (d) and (e).

The difference between the SLPa patterns in Figures 7a and 7b reflects the intensification of the Aleutian Low since 1970 (Figure 7c), consistent with Alexander et al. (2002) and Gan et al. (2017). The intensification of the Aleutian Low is also apparent when 1998 and 2016 strong El Niño winters are excluded from 15 years SLPa differences (Figure S7 in Supporting Information S1), with extreme El Niño intensity anticipated to increase (B. Wang et al., 2019). The strengthened winter atmospheric SLP patterns are associated with increased storminess over the extratropical North Pacific, which results in with both consistently higher mean winter *sHs* and the lack of persistent low *sHs* winters since 1970.

Intensified wave activity is indicated by the occurrence of about twice as many extreme *sHs* events (*sHs* > 5 m) during the 1996–2016 epoch as during 1949–1969 (Figure S8 in Supporting Information S1). SLPa composites

for the two temporal groups of extreme *sHs* events (Figure 7), formed from averages of monthly SLPa when extremes occurred, yield a much deeper low during the 1996–2016 epoch (Figure 7e) compared with 1949–1969 (Figure 7d). These SLPa spatial patterns are consistent with heightened storminess since 1970, which is represented by the SLPa event difference between the two epochs (Figure 7f), and whose location and deeper low indicates increased storm activity nearer the California coast.

Since buoys provide point *Hs* observations, DFM levels arising from regionally averaged wave activity at multiple source areas along the coast and over the continental shelf imply that *sHs* estimates can potentially provide a more robust regional estimate of near-coastal wave variability. Poor correlation of mean winter *sHs* with the Pacific Decadal Oscillation (Mantua & Hare, 2002; $R = 0.10$, p-value $= 0.34$) suggests that sea surface temperature variability alone does not play an important role in winter *sHs* over the extratropical North Pacific. Considering the strong association of winter *sHs* with low SLP over the North Pacific, surprisingly winter *sHs* is also poorly correlated the North Pacific Index (NPI, Trenberth & Hurrell, 1994; $R = -0.11$, p-value $= 0.31$). Elevated wave activity during the 1998 and 2016 winters compared with 1942 and 1958 is consistent with increasing intensity of El Niño events (Lee & McPhaden, 2010), although the MEI is only weakly correlated with winter *sHs* ($R = 0.21$, p-value $= 0.05$). However, heightened winter *sHs* during 1937, 1949, 1950, and 1953 are comparable to recent extreme El Niño winters, implying that other climatological factors associated with global warming play a role in extreme storminess over the extratropical Pacific, which is also consistent with poor correlation of *sHs* with winter NPI over the 1931–2021 epoch. Recent record annual global temperatures (Hansen et al., 2022) suggest that warming may be accelerating, resulting in more strong storms and intimating further increased winter *Hs* may be forthcoming.

6. Conclusions

These results indicate that overall average winter wave conditions can be reproduced from near-coastal historical seismic records, and demonstrate the utility of the methodology presented here for investigating various aspects of the near-coastal ocean wave spectrum in response to climate variability. DFM spectral levels at UC Berkeley seismic station BKS are dominated by near-coastal wave activity. Although microseism levels generally do not give reliable estimates of synoptic *Hs* for extreme wave events, reconstructed mean winter *sHs* closely match buoy observations over common time periods. Winter wave variability is linked to anomalous SLP variability across the extratropical North Pacific basin. The character of decadal variability with increased mean winter *sHs* changed near the advent of the upward trend in anomalous global warming near 1970, with higher mean *sHs* associated with an intensification of the Aleutian Low, consistent with the occurrence of about twice as many extreme *sHs* events during the 1996–2016 epoch compared with 1949–1969. The extreme storm activity across the North Pacific during the 2022–2023 winter may be a harbinger of climate change-induced heightened wave activity along the Pacific Coast. About a 15-year lapse occurred between the 1983, 1998, and 2016 strong El Niños. The apparent developing strong El Niño in 2023–2024 suggests that the frequency of strong El Niños may be increasing, with associated elevated wave heights.

Transformation of digitized analog seismic records from seismic station BKS into wave height estimates, and other long-duration seismic records along the U.S. East Coast, the coast of western Europe, or elsewhere, would allow investigation of the influence of climate change on near-coastal wave climate variability in those regions. This empirical methodology is applicable to near-coastal seismic station—surface buoy pairs. However, digitizing seismograms is expensive. A more efficient digitizing methodology than that used for this study would make other extensive analog seismogram collections available for climate change studies.

Appendix A: Wave Reconstruction From Double-Frequency Microseisms—Methodology

A1. Wave Reconstruction

A1.1. Methodology (From Bromirski & Flick, 2020)

Waves traveling in opposing directions produce a pressure pulse, S_p, that is transformed into seismic Rayleigh surface waves at the seafloor (Longuet-Higgins, 1950). Following Bromirski et al. (1999), S_p at double the wave angular frequency, ω_d, is given by

$$S_P(\omega_d) = \frac{\pi \rho^2 g^2}{2c^2} \omega^3 \, S_w^2(\omega) \, \mathcal{W}_\theta(\omega), \tag{A1}$$

where S_w^2 is the gravity-wave power spectrum of surface displacement (buoy data) at wave frequency ω, ρ the ocean surface density of seawater, g the acceleration due to gravity, c the ocean sound speed, and $\mathcal{W}_\theta(\omega)$ incorporates the wave spectral directional characteristics of both principal and opposing wave fields. The resulting vertical seismic displacement power spectrum at the ocean bottom, S_{ZB}, can be expressed in terms of S_P as

$$S_{ZB}(\omega_d) = R_s(\omega)\, T_{ZB}(\omega_d)\, S_P(\omega_d), \tag{A2}$$

where R_s represents the local active source region of wave-wave interactions and T_{ZB} is the pressure-to-seismic Rayleigh-wave transfer function. Combining Equations A1 and A2 and including a propagation term α_R, the associated vertical PSD S_Z detected by an inland seismometer can be expressed in terms S_w as

$$S_Z(\omega_d) = \frac{\pi \rho^2 g^2}{2c^2} \omega^3 S_w^2(\omega)\, [R_s(\omega) \mathcal{W}_\theta(\omega) T_{ZB}(\omega_d) \alpha_R(\omega_d)], \tag{A3}$$

where α_R represents the Rayleigh wave attenuation under propagation to land.

S_Z (i.e., DFM) levels on land depend on S_w^2 and the terms in brackets, each of which have large uncertainty. Multiple contemporaneous source areas having varying wave conditions and uncertain opposing wave fields make modeling individual synoptic events problematic. To mitigate these issues, the seismic spectra S_Z were adjusted by application of a wave-to-seismic adjustment function T_{ws} (terms in brackets in Equation A3) as:

$$\begin{aligned}
&T_{ws}(\omega_d) = R_s(\omega)\, \mathcal{W}_\theta(\omega)\, T_{ZB}(\omega_d)\, \alpha_R(\omega_d) \\
&S_Z(\omega_d) = T_{ws}(\omega_d)\, S_{ZB}(\omega_d). \quad \text{From Equations 1 and 2, } S_{ZB} \propto S_w^2. \quad \text{Then} \\
&S_Z(\omega_d) \approx T_{ws}(\omega_d)\, S_w^2(\omega), \text{ giving} \\
&T_{ws}(\omega_d) \approx \frac{S_Z(\omega_d)/S_Z(\omega_d)_{\max}}{S_w^2(\omega)/S_w^2(\omega)_{\max}},
\end{aligned} \tag{A4}$$

normalizing the significantly different seismic S_Z and buoy S_w^2 amplitudes by their peak levels. Converting Equation A3 to temporal frequency f, where $\omega = 2\pi f$, and substituting T_{ws} (Equation A4) for the terms in brackets and rearranging, the adjusted (seismic) spectral power $\hat{S}_Z$ is then obtained from

$$\hat{S}_Z(f_d) = \left[\frac{S_Z(f_d)}{\frac{4\pi^4 \rho^2 g^2}{c^2} f^3 T_{ws}(f_d)} \right]^{\frac{1}{2}}, \tag{A5}$$

where f is the ocean gravity-wave frequency, and $f_d = 2f$. Then the equivalent seismic significant wave height, *shs*, is obtained from the band-limited zeroth moment of $\hat{S}_Z$ as

$$shs = 4 \left[\int_{f_1}^{f_2} \hat{S}_Z(f_d)\, df \right]^{\frac{1}{2}}, \tag{A6}$$

where f_1 and f_2 are the analysis band investigated. The seismic-to-wave transfer function, *Tsw*, is obtained from a quadratic least squares fit of *Hs* versus *shs*. Finally, the seismic significant wave height, *sHs*, is determined as $sHs = Tsw * shs$.

Data Availability Statement

National Oceanic and Atmospheric Administration and National Oceanic Data Center, National Oceanic and Atmospheric Administration et al., and Northern California Earthquake Data Center and Berkeley Digital Seismic Network (BDSN).

Acknowledgments
Support for scanning and digitizing of the archived seismograms at UC Berkeley from the former California Dept. of Boating and Waterways is greatly appreciated. Help from Bob Urhammer at UC Berkeley Seismological Laboratory in scanning the historic analog seismograms and providing GAL and SPR instrument response functions was hugely helpful. Thanks to Steve Chuang for his efforts in coding the SeisDig digitizing package. Numerous discussions with Reinhard Flick and Ralph Stephen over the years were invaluable. Thanks to Rick Aster for useful comments on the manuscript.

References

Alexander, M. A., Blade, I., Newman, M., Lanzante, J. R., Lau, N.-C., & Scott, J. D. (2002). The Atmospheric Bridge: The influence of ENSO teleconnections on air–sea interaction over the global oceans. *Journal of Climate*, *15*(16), 2205–2231. https://doi.org/10.1175/1520-0442(2002)015<2205:tabtio>2.0.co;2

Ardhuin, F., Balanche, A., Stutzmann, E., & Obrebski, M. (2012). From seismic noise to ocean wave parameters: General methods and validation. *Journal of Geophysical Research*, *117*(C5), C05002. https://doi.org/10.1029/2011JC007449

Ardhuin, F., Stutzmann, E., Schimmel, M., & Mangeney, A. (2011). Ocean wave sources of seismic noise. *Journal of Geophysical Research*, *116*(C9), C09004. https://doi.org/10.1029/2011JC006952

Aster, R. C., McNamara, D. E., & Bromirski, P. D. (2008). Multidecadal climate-induced variability in microseisms. *Seismological Research Letters*, *79*(2), 194–202. https://doi.org/10.1785/gssrl.79.2.194

Aster, R. C., McNamara, D. E., & Bromirski, P. D. (2010). Global trends in extremal microseism intensity. *Geophysical Research Letters*, *37*(14), L14303. https://doi.org/10.1029/2010GL043472

Bromirski, P. D., & Chuang, S. (2003). *SeisDig: Software to digitize scanned analog seismogram images, user's manual* [Technical Report] (p. 28). Scripps Institution of Oceanography. Retrieved from http://repositories.cdlib.org/sio/techreport

Bromirski, P. D., & Chuang, S. (2023). Berkeley Seismological Laboratory (BSL), pre-1990 scanned seismograms and SeisDig digitizing package [Dataset], [Software]. Retrieved from https://ncedc.org/pub/assembled/BSL_Scanned_Seismogram/

Bromirski, P. D., & Duennebier, F. K. (2002). The near-coastal microseism spectrum: Spatial and temporal wave climate relationships. *Journal of Geophysical Research*, *107*(B8), 2166. https://doi.org/10.1029/2001JB000265

Bromirski, P. D., Duennebier, F. K., & Stephen, R. A. (2005). Mid-ocean microseisms. *Geochemistry, Geophysics, Geosystems*, *6*(4), Q04009. https://doi.org/10.1029/2004GC000768

Bromirski, P. D., & Flick, R. E. (2020). Near-coastal winter waves from microseisms. *Geophysical Research Letters*, *47*(18), e2020GL089831. https://doi.org/10.1029/2020GL089831

Bromirski, P. D., Flick, R. E., & Graham, N. (1999). Ocean wave height determined from inland seismometer data: Implications for investigating wave climate changes in the NE Pacific. *Journal of Geophysical Research*, *104*(C9), 20753–20766. https://doi.org/10.1029/1999jc900156

Bromirski, P. D., Flick, R. E., & Miller, A. J. (2016). Storm surge along the Pacific coast of North America. *Journal of Geophysical Research: Oceans*, *121*(27), 249–251. https://doi.org/10.1029/2012EO270001

Bromirski, P. D., Stephen, R. A., & Gerstoft, P. (2013). Are deep-ocean-generated surface-wave microseisms observed on land? *Journal of Geophysical Research: Solid Earth*, *118*(7), 3610–3629. https://doi.org/10.1002/jgrb.50268

Cayan, D. R., Bromirski, P. D., Hayhoe, K., Tyree, M., Dettinger, M. D., & Flick, R. E. (2008). Climate change projections of sea level extremes along the California coast. *Climatic Change*, *87*(S1), 57–73. https://doi.org/10.1007/s10584-007-9376-7

Elgar, S., Herbers, T. H. C., & Guza, R. T. (1994). Reflection of ocean surface gravity waves from a natural beach. *Journal of Physical Oceanography*, *24*(7), 1503–1511. https://doi.org/10.1175/1520-0485(1994)024<1503:roosgw>2.0.co;2

Gan, B., Wu, L., Jia, F., Li, S., Cai, W., Nakamura, H., et al. (2017). On the response of the Aleutian Low to greenhouse warming. *Journal of Climate*, *30*(10), 3907–3925. https://doi.org/10.1175/JCLI-D-15-0789.1

Gemmrich, J., Thomas, B., & Bouchard, R. (2011). Observational changes and trends in northeast Pacific wave records. *Geophysical Research Letters*, *38*(22), L22601. https://doi.org/10.1029/2011GL049518

Gerstoft, P., & Tanimoto, T. (2007). A year of microseisms in southern California. *Geophysical Research Letters*, *34*(20), L20304. https://doi.org/10.1029/2007GL031091

Grevemeyer, I., Herber, R., & Essen, H.-H. (2000). Microseismological evidence for a changing wave climate in the northeast Atlantic Ocean. *Nature*, *408*(6810), 349–351. https://doi.org/10.1038/35042558

Gualtieri, L., Stutzmann, E., Capdeville, Y., Farra, V., Mangeney, A., & Morelli, A. (2015). On the shaping factors of the secondary microseismic wavefield. *Journal of Geophysical Research: Solid Earth*, *120*(9), 6241–6262. https://doi.org/10.1002/2015JB012157

Guerin, G., Rivet, D., van den Ende, M. P. A., Stutzmann, E., Sladen, A., & Ampuero, J. P. (2022). Quantifying microseismic noise generation from coastal reflection of gravity waves recorded by seafloor DAS. *Geophysical Journal International*, *231*(1), 394–407. https://doi.org/10.1093/gji/ggac200

Gutenberg, B. (1931). Microseisms in North America. *Bulletin of the Seismological Society of America*, *21*, 1–24. https://doi.org/10.1785/bssa0210010001

Gutenberg, B. (1936). On microseisms. *Bulletin of the Seismological Society of America*, *26*(2), 111–117. https://doi.org/10.1785/bssa0260020111

Hansen, J., Sato, M., Simons, L., Nazarenko, S., von Schuckmann, K., Loeb, N. G., et al. (2022). Global warming in the pipeline. *Oxford Open Climate Change*, arXiv:2212.04474, 1–48. https://doi.org/10.48550/arXiv.2212.04474

Hasselmann, K. (1963). A statistical analysis of the generation of microseisms. *Reviews of Geophysics*, *1*(2), 177–210. https://doi.org/10.1029/rg001i002p00177

Haubrich, R. A., & McCamy, K. (1969). Microseisms: Coastal and pelagic sources. *Reviews of Geophysics*, *7*(3), 539–571. https://doi.org/10.1029/rg007i003p00539

Haubrich, R. A., Munk, W. F., & Snodgrass, F. E. (1963). Comparative spectra of microseisms and swell. *Bulletin of the Seismological Society of America*, *53*(1), 27–37. https://doi.org/10.1785/bssa0530010027

IPCC. (2021). Summary for policymakers. In V. Masson-Delmotte, P. Zhai, S. L. Connors, C. Pean, Y. Chen, L. Goldfarb, et al. (Eds.), *Climate change 2021: The physical science basis. Contribution of Working Group I to the sixth assessment report of the Intergovernmental Panel on Climate Change*. Cambridge University Press.

Lee, T., & McPhaden, M. J. (2010). Increasing intensity of El Nino in the central-equatorial Pacific. *Geophysical Research Letters*, *37*(14), L14603. https://doi.org/10.1029/2010GL044007

Longuet-Higgins, M. S. (1950). A theory of the origin of microseisms. *Philosophical Transactions of the Royal Society of London - A*, *243*, 1–35.

Mantua, N. J., & Hare, S. R. (2002). The Pacific decadal oscillation. *Journal of Oceanography*, *58*(1), 35–44. https://doi.org/10.1023/a:1015820616384

Morim, J., Hemer, M., Wang, X. L., Cartwright, N., Trenham, C., Semedo, A., et al. (2019). Robustness and uncertainties in global multivariate wind-wave climate projections. *Nature Climate Change*, *9*(9), 711–718. https://doi.org/10.1038/s41558-019-0542-5

National Oceanic and Atmospheric Administration, & Climate Prediction Center. (2022). Oceanic Nino Index (ONI). Retrieved from https://origin.cpc.ncep.noaa.gov/products/analysis_monitoring/ensostuff/ONI_v5.php

National Oceanic and Atmospheric Administration, & National Oceanic Data Center. Buoy 46013 significant wave height (*Hs*) [Dataset]. Retrieved from https://www.nodc.noaa.gov/BUOY/

National Oceanic and Atmospheric Administration, Physical Sciences Laboratory, & National Centers for Environmental Prediction. NCEP-NCAR reanalysis sea level pressure (SLP) [Dataset]. Retrieved from https://psl.noaa.gov/data/gridded/data.ncep.reanalysis.html

Northern California Earthquake Data Center, & Berkeley Digital Seismic Network (BDSN). Seismic station BKS STS-1 LHZ data, 1992-2021 [Dataset]. https://doi.org/10.7932/BDSN

Obrebski, M. J., Ardhuin, F., Stutzmann, E., & Schimmel, M. (2012). How moderate sea states can generate loud seismic noise in the deep ocean. *Geophysical Research Letters*, *39*(11), L11601. https://doi.org/10.1029/2012GL051896

Reguero, B. G., Losada, I. J., & Méndez, F. J. (2019). A recent increase in global wave power as a consequence of oceanic warming. *Nature Communications*, *10*(1), 205. https://doi.org/10.1038/s41467-018-08066-0

Sierra, J. P., & Casas-Prat, M. (2014). Analysis of potential impacts on coastal areas due to changes in wave conditions. *Climatic Change*, *124*(4), 861–876. https://doi.org/10.1007/s10584-014-1120-5

Stopa, J. E., Ardhuin, F., Stutzmann, E., & Lecocq, T. (2019). Sea state trends and variability: Consistency between models, altimeters, buoys, and seismic data (1979-2016). *Journal of Geophysical Research: Oceans*, *124*(6), 3923–3940. https://doi.org/10.1029/2018JC014607

Storlazzi, C. D., Willis, C. M., & Griggs, G. B. (2000). Comparative impacts of the 1982-83 and 1997-98 El Nino winters on the central California coast. *Journal of Coastal Research*, *16*(4), 1022–1036. ISSN 0749-0208.

Stutzmann, E., Ardhuin, F., Schimmel, M., Mangeney, A., & Tatau, G. (2012). Modelling long-term seismic noise in various environments. *Geophysical Journal International*, *191*(2), 707–722. https://doi.org/10.1111/j.1365-246X.2012.05638.x

Timmermans, B. W., Gommenginger, C. P., Dodet, G., & Bidlot, J.-R. (2020). Global wave height trends and variability from new multi-mission satellite altimeter products, reanalyses, and wave buoys. *Geophysical Research Letters*, *47*(9), e2019GL086880. https://doi.org/10.1029/2019gl086880

Traer, J., & Gerstoft, P. (2014). A unified theory of microseisms and hum. *Journal of Geophysical Research: Solid Earth*, *119*(4), 3317–3339. https://doi.org/10.1002/2013JB010504

Trenberth, K. E., & Hurrell, J. W. (1994). Decadal atmosphere-ocean variations in the Pacific. *Climate Dynamics*, *9*(6), 303–319. https://doi.org/10.1007/BF00204745

Wang, B., Luoa, X., Yang, Y.-M., Sun, W., Cane, M. A., Cai, W., et al. (2019). Historical change of El Niño properties sheds light on future changes of extreme El Niño. *Proceedings of the National Academy of Sciences*, *116*(45), 22512–22517. https://doi.org/10.1073/pnas.1911130116

Wang, X. L., & Swail, V. R. (2001). Changes of extreme wave heights in northern hemisphere oceans and related atmospheric circulation regimes. *Journal of Climate*, *14*(10), 2204–2221. https://doi.org/10.1175/1520-0442(2001)014<2204:coewhi>2.0.co;2

Wang, X. L., & Swail, V. R. (2006). Climate change signal and uncertainty in projections of ocean wave heights. *Climate Dynamics*, *26*(2–3), 109–126. https://doi.org/10.1007/s00382-005-0080-x

Wolter, K., & Timlin, M. S. (2011). El Nino/Southern Oscillation behaviour since 1871 as diagnosed in an extended multivariate ENSO index (MEI.ext). *International Journal of Climatology*, *31*(7), 1074–1087. https://doi.org/10.1002/joc.2336